INORGANIC CHEMISTRY FRONTIERS

RESEARCH ARTICLE

View Article Online
View Journal | View Issue

Cite this: *Inorg. Chem. Front.*, 2024, **11**, 7910

Rationally reconstructing the surface microstructure of a chemical bath deposited electron transport layer for efficient and stable perovskite solar cells†

Xinxuan Yang,[a,b,c,d] Lexin Wang,[c] Meihan Liu,[c] Jiahui Jin,[c] Lili Yang,[c,d] Lin Fan,[c,d] Maobin Wei,[c,d] Huilian Liu,[c,d] Haoran Chen,[a,b] Jinghai Yang,*[c,d] Yulei Chang*[a,b] and Fengyou Wang*[c,d]

In perovskite solar cells (PSCs), chemical bath deposition (CBD) is promising as the core technique for preparing a commercial electron transport layer (ETL) because the film prepared by CBD exhibits excellent uniform and conformal coverage of the substrate. However, metal oxide (MO_x) films prepared through CBD often have defects on the surface like oxygen vacancies and hydroxyl that limit the PSCs efficiency and degrade the long-term stability. To address this obstacle to the scaled PSCs application, we here reconstructed the surface microstructure of a CBD tin dioxide (SnO_2) ETL by post-treatment with dilute H_2SO_4 solution to terminate the oxygen vacancies from the MO_x surface while effectively removing the hydroxyl groups. Concurrently, the potent oxidizing property of H_2SO_4 facilitates the transformation from Sn(II) to Sn(IV), thereby enhancing the alignment of the energy level between SnO_2 and the perovskite (PVK) layer within the ETL architecture. Moreover, the interaction between SO_4^{2-} and the perovskite precursor mitigates the difference in crystallization velocity between the perovskite upper and buried surfaces, enabling the formation of films with homogeneous phase distribution and good crystallization. Ultimately, with the assistance of this facile surface microstructure reconstruction, the power conversion efficiency (PCE) improves from 22.48% to 24.29%.

Received 20th July 2024,
Accepted 25th September 2024

DOI: 10.1039/d4qi01808g

rsc.li/frontiers-inorganic

1. Introduction

In the past decade, perovskite solar cells (PSCs) have achieved remarkable advancements with the latest certified maximum power conversion efficiency (PCE) beyond 26.1%.[1] A typical planar heterojunction PSCs device comprises five parts: a transparent conductive substrate, an electron transport layer (ETL), a perovskite layer, a hole transport layer (HTL), and an electrode. The ETL directly interfaces with the perovskite layer to extract and transport photogenerated electrons, block holes, and inhibit carrier recombination.[2] The efficiency of electron extraction and collection, the hysteresis phenomenon in the *I–V* test, and the long-term stability of the device are all closely associated with the optical–electrical characteristics of the ETL itself.[3] To further advance the practical development of PSCs and expand their applications, it is particularly crucial to develop facile processes for large-scale preparation of ETLs.

Currently, the most commonly used materials for ETLs are various inorganic metal oxides (MO_x), such as SnO_2, TiO_2, and ZnO.[4] These materials are favored due to their higher electron mobility, low cost, good stability, and compatibility with the energy levels of perovskites.[5] To prepare these MO_x thin films, atomic layer deposition (ALD), spin coating, and chemical bath deposition (CBD) are three commonly utilized methods.[6] Each of these preparation methods has specific characteristics; for example, the ALD method enables precise control over film thickness while achieving high substrate coverage rates and excellent uniformity. However, this process is time-consuming as it requires a high vacuum environment and specific precursor materials, limiting its suitability for large-scale or mass production applications. In laboratory settings, spin coating remains the most frequently employed technique for preparing

[a]*Key Laboratory of Luminescence Science and Technology, Chinese Academy of Sciences & State Key Laboratory of Luminescence Science and Applications, Changchun Institute of Optics, Fine Mechanics and Physics, Chinese Academy of Sciences, Changchun 130033, Jilin, China. E-mail: yuleichang@ciomp.ac.cn*
[b]*University of Chinese Academy of Sciences, Beijing 100049, China*
[c]*Key Laboratory of Functional Materials Physics and Chemistry of the Ministry of Education, Jilin Normal University, Changchun 130103, China. E-mail: jhyang1@jlnu.edu.cn, wfy@jlnu.edu.cn*
[d]*National Demonstration Center for Experimental Physics Education, Jilin Normal University, Siping 136000, China*

†Electronic supplementary information (ESI) available. See DOI: https://doi.org/10.1039/d4qi01808g

MO_x films. This method has a simple process and high repeatability, but it is difficult to prepare a uniform large-area film, which also limits its commercial development. In contrast, the film prepared by the CBD method exhibits strong uniformity with fewer pinholes and can achieve conformal coverage of the substrate.[7,8] This method not only offers high efficiency and low cost but also demonstrates excellent repeatability, adaptability, and suitability for large-scale production.[9] In 2016, Correa-Baena *et al.* successfully applied CBD technology to deposit a SnO_2 layer in flat PSCs. They achieved a low voltage loss of 0.41 V and obtained a stable PCE of 20.7%.[10] In 2021, Jason *et al.* conducted a detailed analysis of the changes in product composition, thickness, and coverage during the deposition of SnO_2 using CBD due to chemical reactions. They successfully prepared a high-quality SnO_2 film and achieved an efficiency breakthrough of 25.2%.[11] This suggests that CBD-SnO_2 could potentially improve the photovoltaic efficiency of devices even further. However, inevitable defects on the surface like oxygen vacancies (V_O) and hydroxyl groups (–OH) will be generated on the CBD-MO_x film, which limits the further development of CBD-SnO_2. These defects not only increase non-radiative recombination and reduce the crystal quality of perovskite thin films but also accelerate device degradation.[12]

To address this issue, researchers have developed various surface modification schemes (organic base interface layers,[13,14] inorganic salts,[15,16] carbon-based inorganic materials,[17,18] and perovskite materials[19]) for MO_x films, to passivate interface defects, adjust band arrangements, and control perovskite crystallization. To be specific, mercaptosuccinic acid,[20] ammonium fluoride,[21] 4-fluorothiophenol[13] and other materials can provide active groups that react with the terminal –OH of the CBD-SnO_2 surface. The resulting reaction product is then separated during subsequent annealing treatment, thereby reducing the concentration of –OH on the film surface. Furthermore, the introduction of periodic acid,[9] potassium permanganate[12] and other inorganic salts can not only remove the surface –OH of CBD-SnO_2 from the neutralization reaction with hydrogen ions (H^+), but also promote the transformation from Sn(II) to Sn(IV) on the surface through its strong oxidation, reduce the density of defect sites and improve the energy level arrangement. In addition, the ETL/perovskite interface can form an oxygen bridge by introducing different oxygen-containing metal salts.[22] However, the passivation materials utilized in the aforementioned methods will introduce additional impurity ions or groups, thereby influencing the distribution of electric fields within the device.[23]

Accordingly, rational manipulation of the surface microstructure of the CBD ETL to mitigate the energy loss at the ETL/perovskite interface is urgently required. In this work, we synergistically terminated the surface traps and eliminated the –OH on the CBD-SnO_2 ETL surface by assembling SO_4^{2-} and generating a hydration reaction on the CBD-SnO_2 ETL surface. Sulfuric acid (H_2SO_4), known for its acidic and highly oxidizing properties, was employed due to its ability to achieve multifunctional modification at the ETL/perovskite interface without introducing additional cationic impurities. The H^+ in H_2SO_4 solution can not only react with the surface –OH of the SnO_2 film to play a deprotonation role, but also its strong oxidation can oxidize Sn-II (SnO) to Sn-IV (SnO_2), reaching a more optimal energy level matching between the CBD-SnO_2 and perovskite. At the same time, the SO_4^{2-} ion has a tetrahedral structure consisting of four identical sulfur–oxygen bonds. This self-dual structure with the properties of the sulfuryl group can be maintained at the interface through strong interactions with SnO_2 and the perovskite layer, forming an interfacial oxygen bridge, improving the crystal quality of the perovskite film, and optimizing the charge transport at the interface.[15,24] These benefits enable and improve the photovoltaic performance of PSCs with a champion PCE of 24.29%.

2. Results and discussion

Fig. 1 illustrates the preparation process of SnO_2 films *via* CBD and interfacial modification using H_2SO_4 solution. Following thorough cleaning, the purchased FTO glass is immersed in an aqueous solution containing stannous chloride dihydrate, urea, hydrochloric acid, and thioglycolic acid. Subsequently, it is subjected to a 4 hour heating period in a water bath at 90 °C. The residual reagents on the film surface are then eliminated through ultrasonic cleaning with deionized water and isopropyl alcohol before annealing at 150 °C for 1 hour. In the case of the CBD-SnO_2 film modified with H_2SO_4 solution (CBD-SSO), after cooling to room temperature, it undergoes direct spin coating with varying concentrations of H_2SO_4 solutions followed by annealing at 150 °C for 15 min.

The surface morphologies of CBD-SnO_2 and CBD-SSO were investigated using scanning electron microscopy (SEM) and atomic force microscopy (AFM). SEM and AFM images reveal no significant alterations in the surface morphology and roughness following H_2SO_4 surface modification (Fig. S1a and b ESI†). The optical transmission spectra of both CBD-SnO_2 and CBD-SSO films exhibit similar transmittance within the 300–800 nm range (Fig. S2, ESI†). To examine the impact of H_2SO_4 on the charge transfer characteristics of the ETL, we investigated the conductivity and electron mobility of the FTO/ETL/Ag device using the space charge limited current (SCLC) method (Fig. 2a and b ESI Note S1†).[25,26] The CBD-SSO film exhibited an increase in conductivity from 2.37×10^{-6} S m^{-1} to 3.15×10^{-6} S m^{-1}. Additionally, based on the $J^{1/2}$–V curve depicted in Fig. 2b, it can be observed that the electron mobility of the CBD-SSO film (5.99×10^{-15} m^2 V^{-1} s^{-1}) surpasses that of the CBD-SnO_2 film (4.25×10^{-15} m^2 V^{-1} s^{-1}). The enhanced conductivity and electron mobility exhibited by CBD-SSO films suggest the advantageous nature of this approach for facilitating efficient electron extraction and transport. Measurements of the Hall effect yield similar findings (Fig. 2c). In comparison with the CBD-SnO_2 film (μ_H = 20.31 cm^2 V^{-1} s^{-1}, $n = 1.16 \times 10^{22}$ cm^{-3}), CBD-SSO films exhibit an elevated Hall mobility μ_H (27.39 cm^2 V^{-1} s^{-1}) and a higher carrier concentration ($n = 1.83 \times 10^{22}$ cm^{-3}).

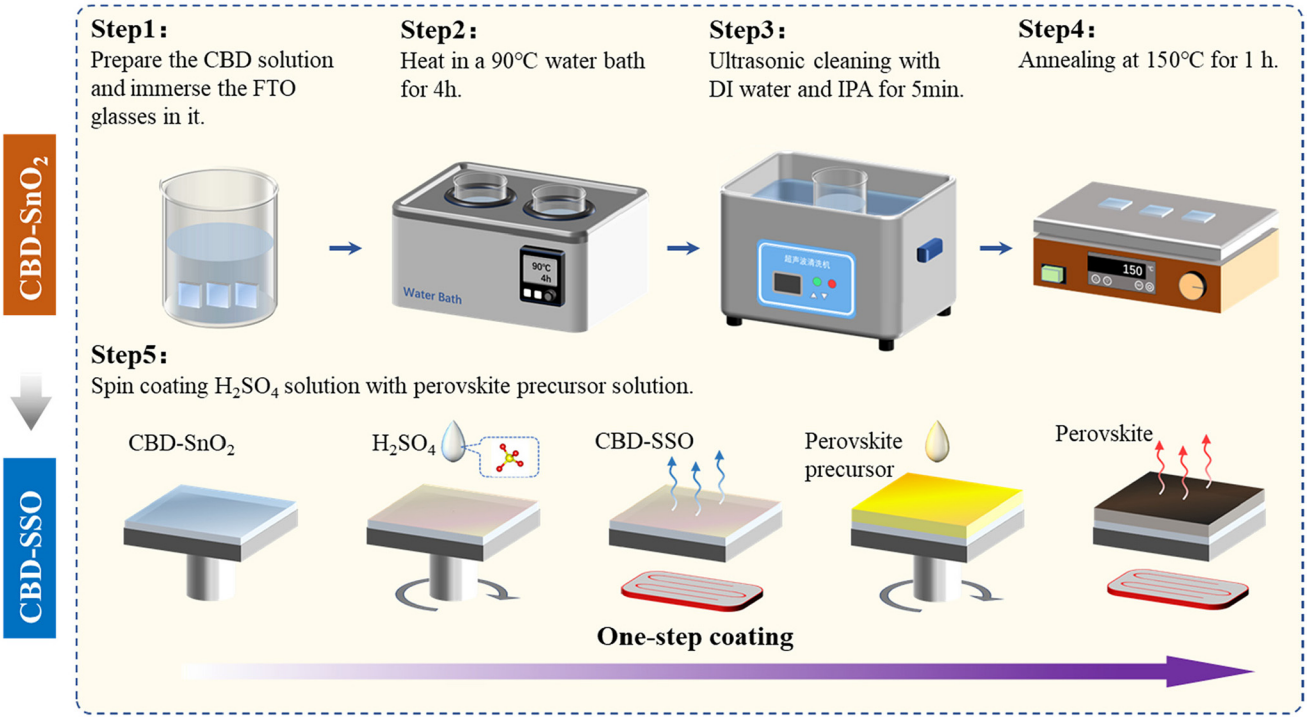

Fig. 1 Schematic illustration of preparing CBD-SnO_2, CBD-SSO, and the perovskite film deposited on different ETLs.

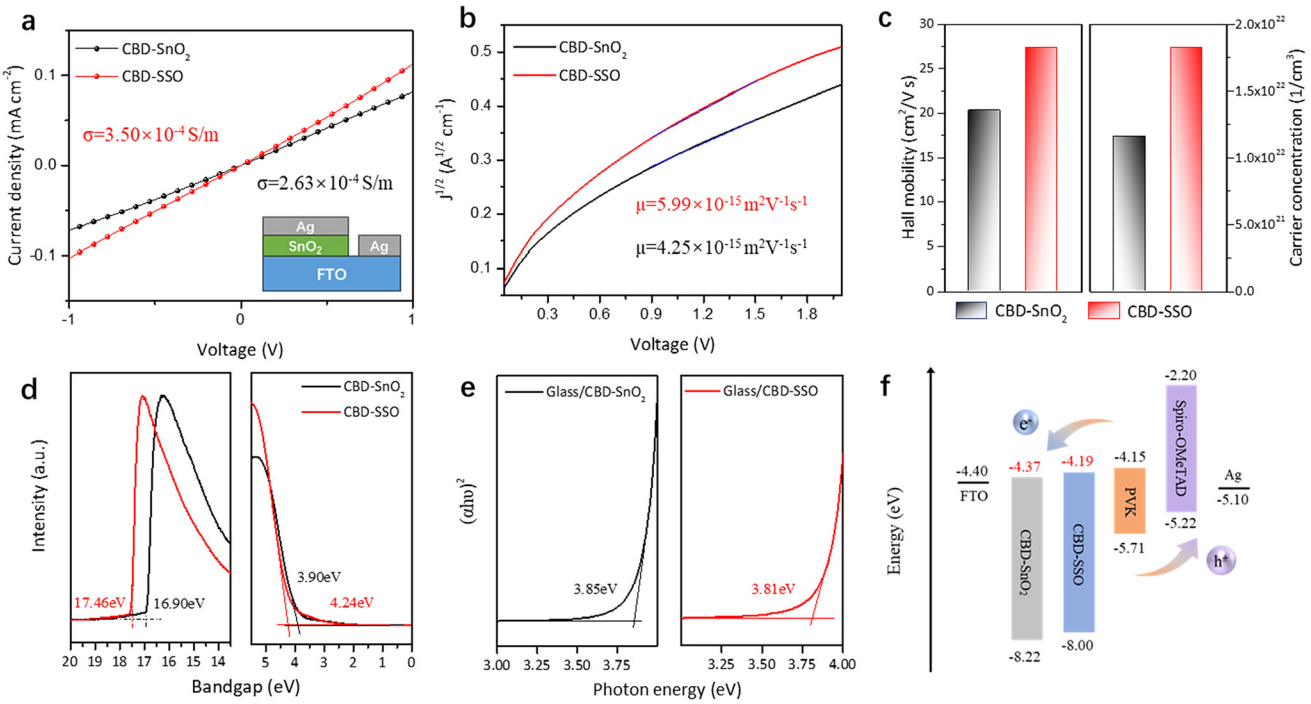

Fig. 2 *J–V* curves of the devices for evaluating the (a) conductivity and (b) mobility of CBD-SnO_2 and CBD-SSO. (c) Hall mobility and carrier concentration results of the pristine CBD-SnO_2 and CBD-SSO films. (d) UPS spectra of secondary electron cut-off and valence bands for CBD-SnO_2 and CBD-SSO, respectively. (e) Tauc plots of the pristine CBD-SnO_2 and CBD-SSO films. (f) Schematic energy level diagram of CBD-SnO_2 and CBD-SSO compared with that of the perovskite.

Subsequently, the impact of H_2SO_4 modification on the energy band structure of the thin films was investigated using ultraviolet photoelectron spectroscopy (UPS) (Fig. 2d). The valence band maximum (VBM) value of the sample can be calculated using the formula: VBM = 21.22 eV − E_{cutoff} + E_{onset}. Combined with the optical band gap values of the sample (Fig. 2e), the VBM values of CBD-SnO_2 and CBD-SSO are 8.22 eV and 8.00 eV, respectively. The conduction band minimum (CBM) values of these materials are 4.37 eV and 4.19 eV. Consequently, the energy level diagram of the CBD-SnO_2 and CBD-SSO devices is presented in Fig. 2f. The upward shift of the conduction band and Fermi level of SnO_2 enables a more favorable band alignment between CBD-SSO and the perovskite layer, resulting in reduced energy barriers at the ETL/perovskite interface and will enhance electron extraction at the interface.

We first used X-ray photoelectron spectroscopy (XPS) to study the causes of the phenomenon. As depicted in Fig. 3a, a peak at ~168 eV corresponding to S of SO_4^{2-} was observed on the CBD-SSO film, suggesting the presence of SO_4^{2-} on the surface. The Sn 3d XPS scan (Fig. 3b) reveals a shift in the positions of the two peaks corresponding to Sn $3d_{5/2}$ and $3d_{3/2}$, from 487.2 and 495.6 eV (CBD-SnO_2) to higher binding energies of 487.6 and 496.1 eV (CBD-SSO), respectively. Fig. 3c shows the Fourier transform infrared (FTIR) spectra of CBD-SnO_2 and CBD-SSO, respectively. Two peaks (~1050 cm^{-1} and 600 cm^{-1}) attributed to the symmetric stretching vibration (V_{s-o}) and symmetric asymmetric bending (δ_{s-o}) of the S–O bond in SO_4^{2-}, exhibit a redshift in CBD-SSO. Meanwhile, the set of S–O vibrations was not detected in the CBD-SnO_2 film. These experimental results indicate that there is an interaction between Sn^{4+} and SO_4^{2-}, and the increase in binding energy of Sn 3d suggests a transformation from Sn(II) to Sn(IV).[12] Subsequently, O 1s in XPS was analyzed. As depicted in Fig. 3d and e, the peaks at around 532.5, 532.8, and 531.1 eV can be

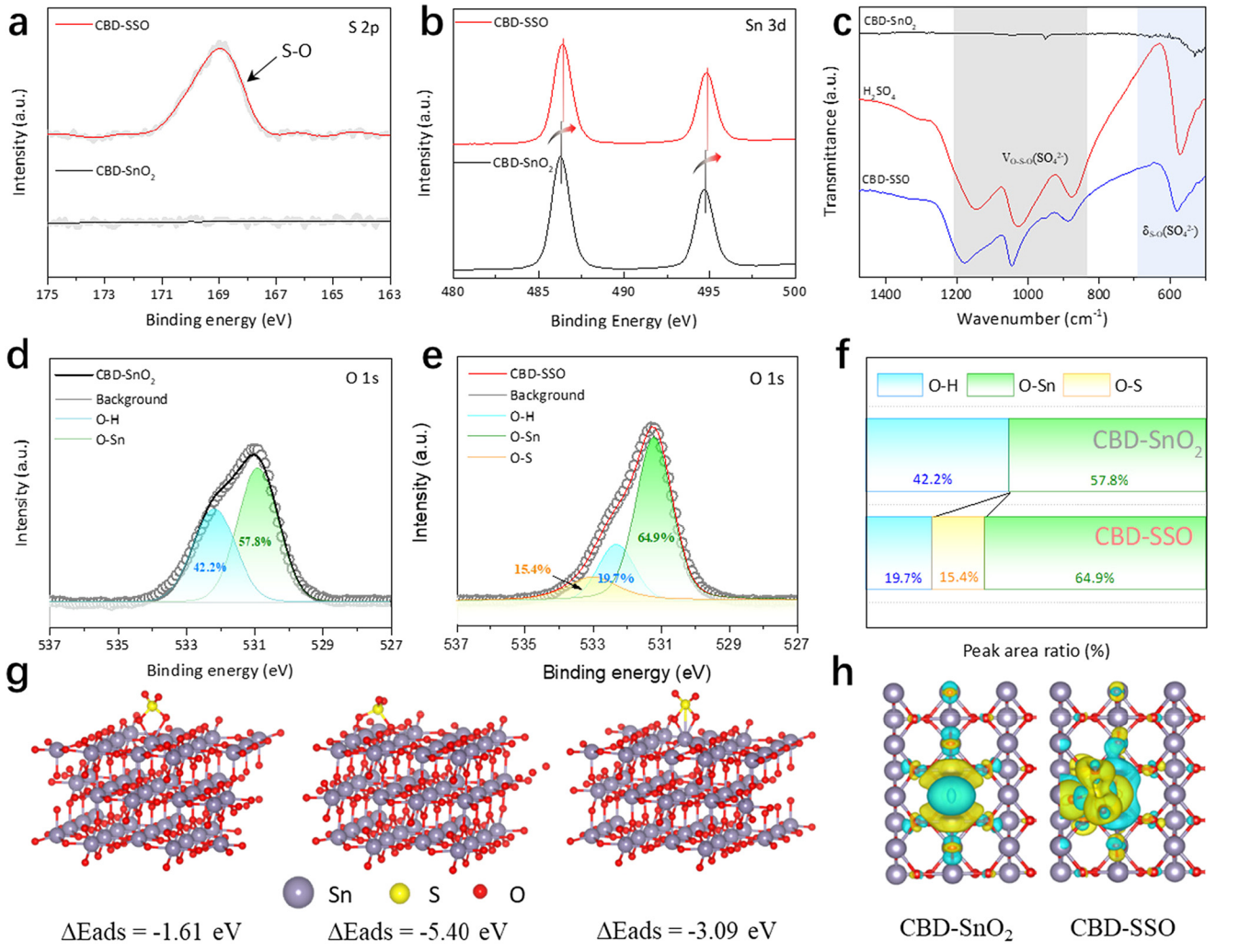

Fig. 3 XPS of (a) S 2p, (b and c) O 1s (hollow circle: raw data; line: fitted data), and (d) Sn 3d for the CBD-SnO_2 and CBD-SSO films. Absorption energy and corresponding structures. (e) FTIR spectra for CBD-SnO_2 and CBD-SSO films. (f) XPS spectra of Pb 4f for PVK and PVK + H_2SO_4. (g) Schematic diagram illustrating SO_4^{2-} adsorption at various positions on the CBD-SnO_2 surface. (h) Charge density difference of SO_4^{2-} on the CBD-SnO_2 (110) surface at an isosurface of 1.5 × 10^{-3} e $Å^{-3}$.

attributed to –OH, SO_4^{2-}, and the oxygen within saturated lattices, respectively. Compared with CBD-SnO_2, a peak of the S–O bond appeared in CBD-SSO, further indicating the successful introduction of SO_4^{2-}. Concurrently, the proportion of the –OH peak area decreased from 42.2% to 15.4%, while the content of lattice oxygen increased from 57.8% to 64.9% (Fig. 3f), indicating more chemisorbed non-lattice oxygen transferring to lattice oxygen as SnO_2.[27] The increase in the water contact angle on the film surface further confirms that SO_4^{2-} modification reduces the –OH content on the surface of MO_X, leading to a change in the Gibbs free energy on the surface of MO_X (Fig. S3†). It is widely acknowledged that the presence of surface –OH groups introduces deeper energy levels within the band gap proximal to the valence band, thereby leading to non-radiative recombination and energy dissipation in the device.[28,29] Our surface micro-reconstruction method can effectively reduce the –OH content on the MO_x surface, which is of great significance for improving the PCE and stability of PSCs based on CBD-MO_x. In addition, we also performed SO_4^{2-} modification on other widely used MO_X ETL surfaces and compared the XPS test results. Fig. S4† illustrates the O 1s scan of titanium oxide prepared *via* the CBD method (CBD-TiO_2) and SnO_2 prepared through the spin coating method (SP-SnO_2) before and after H_2SO_4 treatment, respectively. The results demonstrate that H_2SO_4 treatment can effectively reduce the –OH content on the MO_X film surfaces to varying degrees. These findings suggest that our proposed surface microstructure reconstructing strategy possesses universality in preparing ETLs for PSCs.

We conducted density functional theory (DFT) calculations to clarify whether SO_4^{2-} will remain at the –OH site and occupy V_O. According to the existing research findings, the surface of CBD-SnO_2 films at this stage exhibits four types of commonly observed oxygen defects.[30] These include two –OH defects and two V_O defects: (1) terminal hydroxyl (O_{HT}), which refers to a single hydroxyl group binding to a single Sn atom on the surface of SnO_2; (2) bridged hydroxyl group (O_{HB}), consisting of a bridged oxygen and an adsorbed hydrogen atom; (3) bridging oxygen vacancy (V_{OB}), indicating the absence of bridging oxygen atoms; and (4) deep oxygen vacancy (V_{OD}), representing the absence of another oxygen atom located deeper than bridged oxygen. We chose the thermodynamically most stable (110) crystal plane as the study surface (detailed approach in the ESI Note S2†). The absorption energies (E_a) of SO_4^{2-} adsorbed at terminal Sn, O_{HB} (V_{OB}), and V_{OD} are −1.61, −5.40, and −3.09 eV, respectively (Fig. 3g). The negative E_a values indicate that SO_4^{2-} can easily adsorb on these sites, effectively passivating the defects. A more negative E_a means that SO_4^{2-} is more likely to be adsorbed by the bridged oxygen site. The differential charge density distribution of SO_4^{2-} before and after adsorption to O_{HB} and V_{OB} is illustrated in Fig. 3h. Blue regions indicate electron depletion following charge redistribution, while yellow regions represent electron accumulation. It can be observed that the interaction between the SnO_2 film and SO_4^{2-} alters the charge distribution on the ETL surface. When SO_4^{2-} was adsorbed on the ETL surface, scattered electron clouds appeared in the unbonded part, indicating that adsorption not only filled the V_O, but also improved the electrical conductivity.[31]

Subsequently, perovskite films were deposited on CBD-SnO_2 and CBD-SSO substrates (referred to as CBD-SnO_2-PVK and CBD-SSO-PVK, respectively) to examine how various substrates affect the shape and growth characteristics of perovskites. Top-view SEM images showed that the overall surface morphology of CBD-SSO-PVK remained almost unchanged (Fig. 4a and b); however, the average grain size of the perovskite films increased from ~1.91 μm to ~2.75 μm following such treatment. AFM test results indicated that CBD-SSO reduced the RMS roughness of the perovskite film from 10.9 to 9.1 nm (Fig. S5, ESI†). The crystal structure of perovskite films on different ETL substrates was characterized using an X-ray diffractometer (XRD) (Fig. 4c). The intensity of the two main diffraction peaks corresponding to the (100) and (110) planes of CBD-SSO-PVK experienced a notable rise, indicating an enhancement in perovskite crystallinity. Furthermore, to investigate the carrier recombination and carrier transport dynamics between the ETL and perovskite, steady-state photoluminescence (PL) and time-resolved photoluminescence (TRPL) spectra were characterized (Fig. 4d). The PL signal observed at CBD-SSO-PVK was significantly reduced, suggesting that CBD-SSO demonstrates enhanced electron extraction efficacy from the active layer. The TRPL curve was modeled using a function that represents double exponential decay, and CBD-SSO-PVK has a shorter τ_{avg} (6.06 ns) compared to CBD-SnO_2-PVK (12.65 ns). Please refer to Table S1 of the ESI† for specific details regarding related parameters. Subsequently, we conducted an optimization of the concentration of H_2SO_4 solution (Fig. S6†). By comparing the results of PL and TRPL, it can be concluded that a 0.5 M H_2SO_4 solution is more conducive to promoting the charge transfer between the CBD-SnO_2 and perovskite. The subsequent characterization of CBD-SSO-PVK was based on this concentration, and the samples were referred to as "control" and "target" before and after treatment with a H_2SO_4 solution, respectively. We also measured the dark current density–voltage (*J–V*) characteristics of the devices with a structure of FTO/CBD-SnO_2/perovskite/PCBM/Ag to estimate the defect density of the perovskite films (Fig. 4f). A typical dark *J–V* curve can be divided into three regions: the ohmic region, the defect-filling limited (TFL) region, and the no-trap space charge limited current region. The electron defect state density (N_t) can be estimated from the voltage at which defect filling is limited (V_{TFL}).[32,33] Compared with the control film (V_{TFL} = 0.409 V, N_t = 5.08×10^{15} cm^{-3}), the target film showed a lower V_{TFL} value of 0.324 V and a lower N_t value of 4.02×10^{15} cm^{-3}, respectively.

To elucidate the causes of the above-mentioned effects, we first conducted XPS testing to determine the interaction between the perovskite and SO_4^{2-}. As depicted in Fig. 5a, the Pb 4f of PbI_2 in pure perovskite films exhibits two prominent peaks at 137.98 and 142.88 eV, corresponding to Pb $4f_{7/2}$ and Pb $4f_{5/2}$, respectively. In the target sample, the positions of these peaks shift to 139.08 and 143.88 eV, indicating an inter-

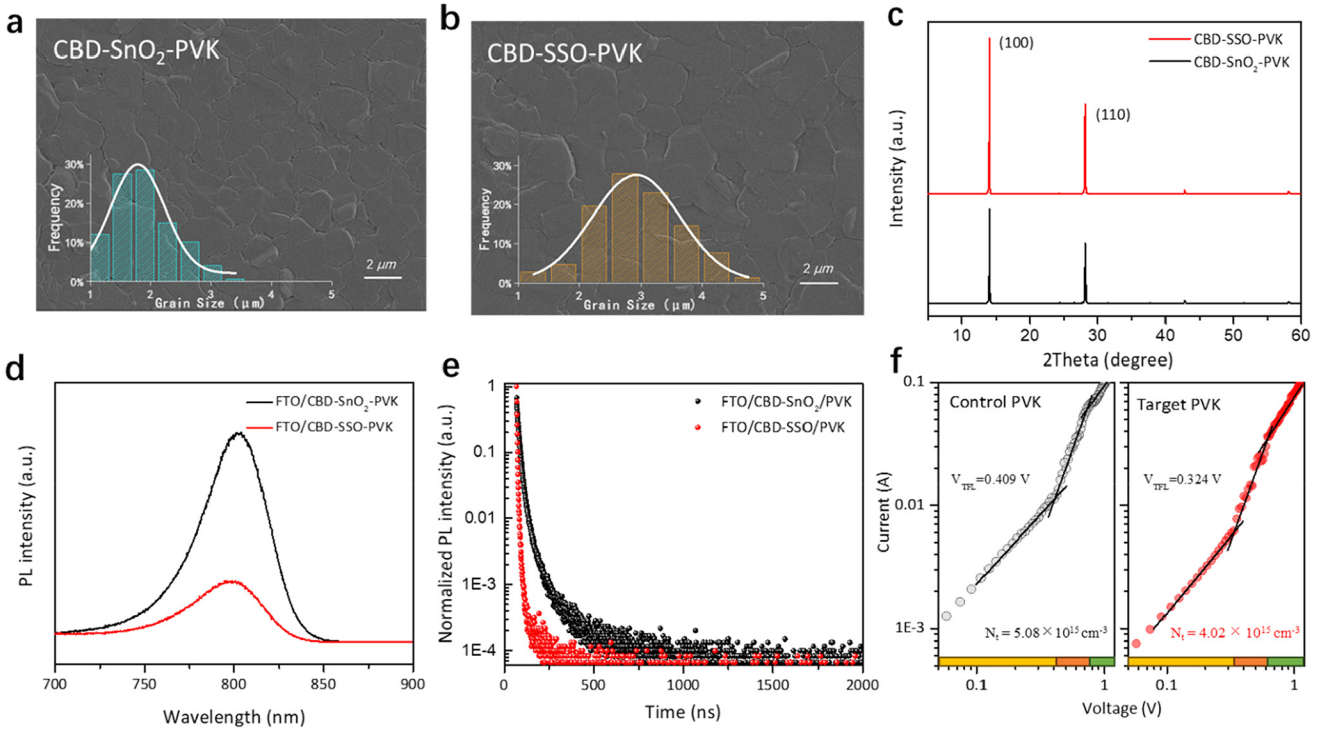

Fig. 4 (a and b) SEM images of CBD-SnO_2-PVK and CBD-SSO-PVK. The inset shows the grain size distributions of 100 crystal particles of CBD-SnO_2-PVK and CBD-SSO-PVK. (c) XRD patterns of CBD-SnO_2-PVK and CBD-SSO-PVK. (d and e) PL spectra and time-resolved PL (TRPL) spectra of FTO/CBD-SnO_2-PVK and FTO/CBD-SSO-PVK, respectively. (f) The space-charge-limited-current (SCLC) curves of the electron-only devices (FTO/ETL/PVK/PCBM/Ag) based on CBD-SnO_2 and CBD-SSO ETLs.

action between PbI_2 and SO_4^{2-}. The UV absorption peak of PbI_2 decreases significantly when SO_4^{2-} is introduced, confirming the interaction between SO_4^{2-} and PbI_2 (Fig. S7†).[34]

In situ temperature change XRD tests were conducted to explain the effect of SO_4^{2-} modification on the crystallization kinetics of the perovskite (Fig. 5b and c). Compared to the control film, the (100) diffraction peak intensity of the target film shows a slower increase, and the half-peak width further narrows, with the increase in temperature. This shows that the crystallization speed of the target film is lower than that of the control film, and the grain size is larger. At the same time, the diffraction intensity of the δ-phase in the target sample is lower and disappears faster. The photographs in Fig. 5d illustrate a comparison between control and target perovskite films annealed at 100 °C. The control film initiates the transformation into the black phase at 6 s and completes it by 12 s. In contrast, the target film exhibits a phase transition time of 12 s and complete transformation to the black phase in 21 s. It is evident that the crystallization rate of the target film is significantly reduced.

In summary, strong interaction can be seen between SO_4^{2-} fixed on the surface of SnO_2 and the hexahedral structure of PbI_2 in the perovskite precursor, thus changing the crystallization kinetics of the film. The slower nucleation process reduces the number of crystal nuclei and promotes the formation of larger grains. In addition, the strong adsorption between SO_4^{2-} and the perovskite contributes to the formation of a dense and void-free interface, thereby making the perovskite film more uniformly dense with fewer defects (Fig. 5e and f).

Then we fabricated the n-i-p type PSCs with structure of glass/FTO/CBD-SnO_2 (or CBD-SSO)/perovskite($FAPbI_3$)/Spiro-OMeTAD/Ag. Fig. 6a and b illustrate the current density–voltage (J–V) curve for both the control and target devices. The control device achieved a PCE of 22.48% with an open circuit voltage (V_{oc}) of 1.20 V, a short circuit current density (J_{sc}) of 23.38 mA cm^{-2}, and a fill factor (FF) of 80.19%. The optimal target device has a PCE of 24.29%, a V_{oc} of 1.23 V, a J_{sc} of 24.29 mA cm^{-2}, and an FF of 81.61%. Among them, the V_{oc} and FF exhibited improvements. The increased V_{oc} is attributed to the suppression of non-radiative recombination losses, resulting from the appropriate energy level alignment and the reduction of defect recombination at the interface. Fig. 6c illustrates the statistical PCE values of 20 devices, with average PCE values of 21.51% for control devices and 23.39% for target devices, respectively. As is evident from the external quantum efficiency (EQE) spectrum depicted in Fig. 6d, the target devices exhibit slightly higher EQE values in the 360 to 900 nm range compared to the control devices. Simultaneously, the integrated J_{sc} value increases from 22.26 mA cm^{-2} to 23.01 mA cm^{-2}, both of which are consistent with the J_{sc} value in Fig. 6a and b. The stable current density

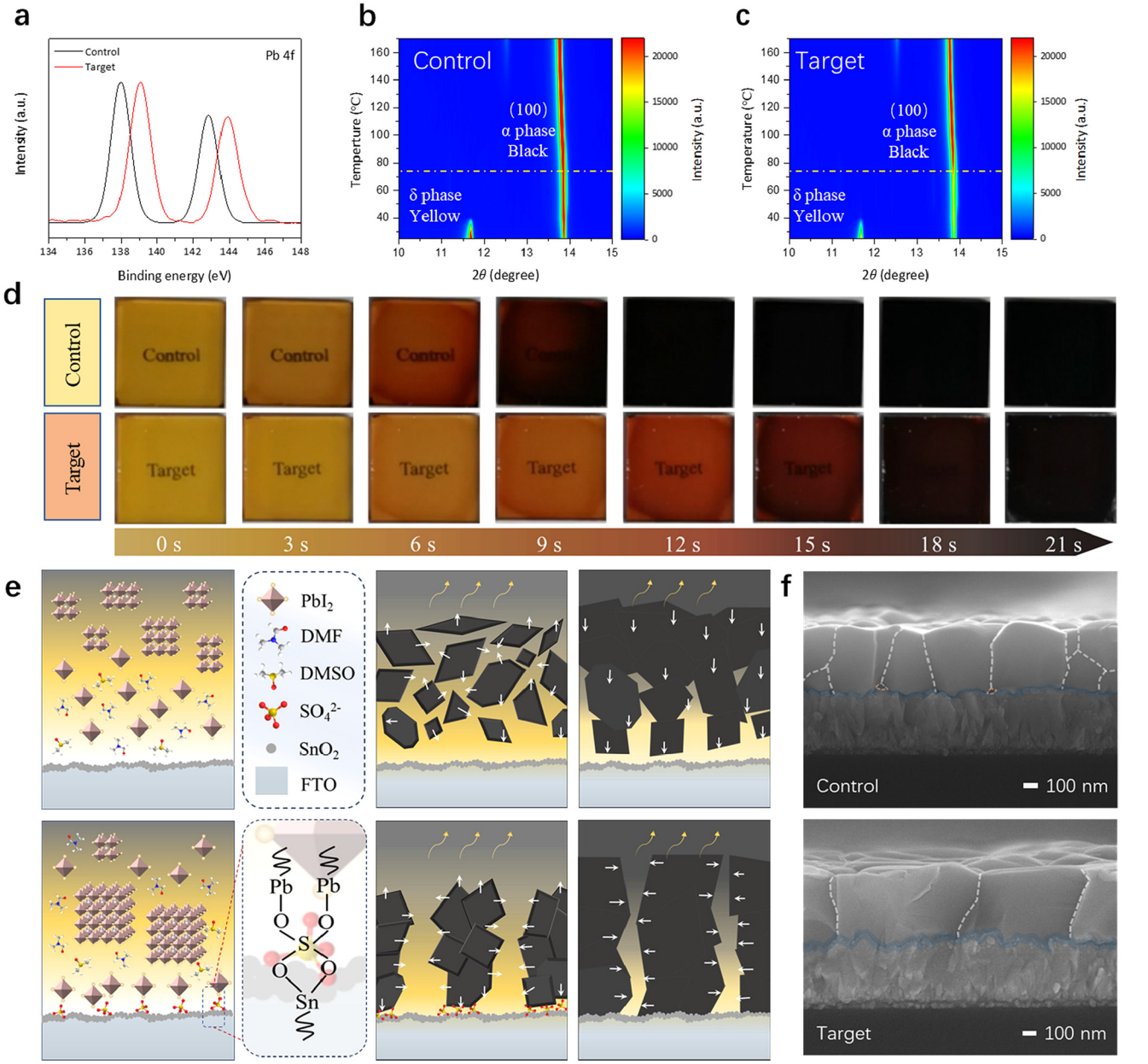

Fig. 5 (a) XPS of Pb 4f of the perovskite with H_2SO_4 or not. (b) XRD contours of the control and (c) target films with *in situ* temperature change. (d) Color change of the perovskite film with annealing time at 100 °C. (e) Crystallization of the perovskite on different CBD-SnO_2 substrates. (f) Cross-sectional SEM images of the complete devices.

and power output at the maximum power point (MPP) were then tested for both the control and target devices under AM 1.5G illumination (Fig. 6e). The steady power output (SPO) of the target device reached 22.91% within 100 seconds, with a steady-state current density of 22.29 mA cm^{-2}. This enhanced photovoltaic performance further confirms that micro-reconstruction of the CBD-SnO_2 surface is an effective and universally applicable strategy. Then, to further clarify the mechanism behind the enhancement of device performance, electrochemical impedance spectroscopy (EIS) measurements were conducted to characterize the interfacial charge transfer dynamics of both devices. As depicted in Fig. S8,† under dark conditions with a bias of 1 V, a Nyquist diagram was obtained. Generally, charge transfer resistance (R_{ct}) is associated with a high frequency range while compound resistance (R_{rec}) is related to a low frequency range. The R_{ct} of the target device is lower than that of the control device, indicating superior charge transport performance in the former case. Additionally, compared to the control device, an increase in R_{rec} confirms a reduced carrier recombination rate. According to the Mott–Schottky analysis (Fig. 6f), the built-in potential (V_{bi}) of the target device (1.07 V) exceeds that of the control device (0.94

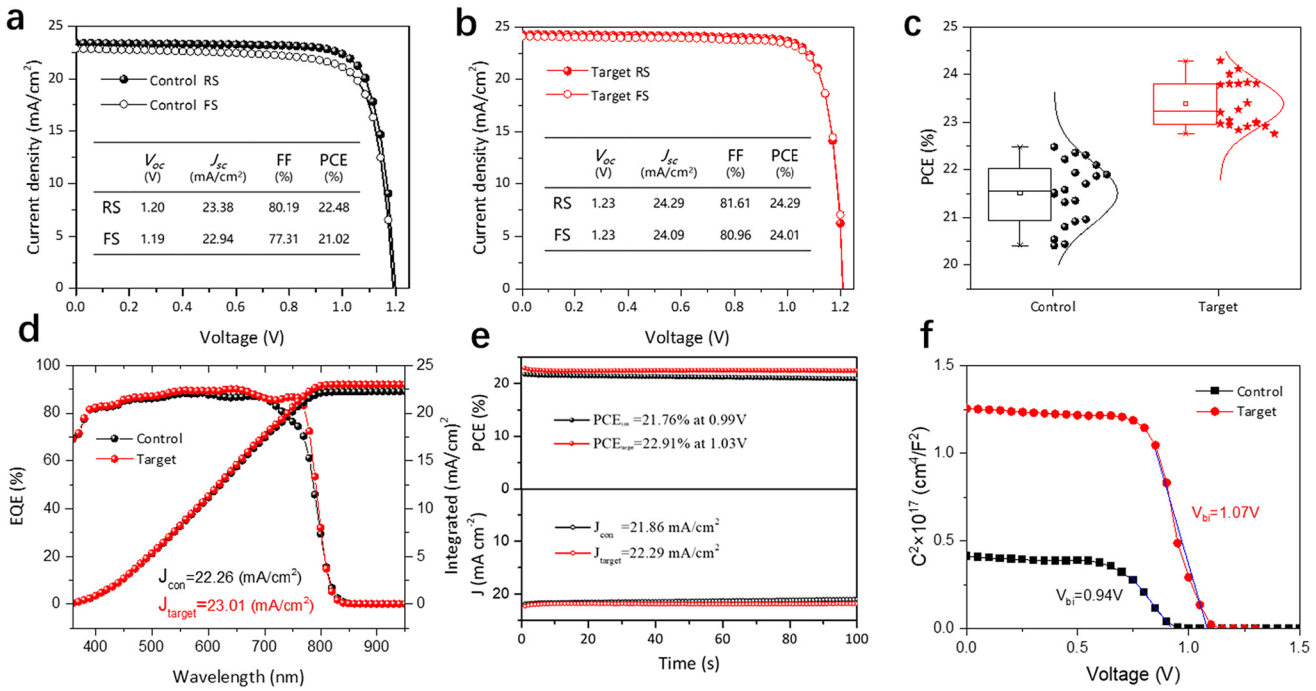

Fig. 6 The champion *J*–*V* curves of (a) the control and (b) target devices with an active area of 0.09 cm^2. (c) The PCE statistical diagram for the control and target devices. (d) EQE spectra. (e) The steady-state efficiency of the devices and (f) Mott–Schottky plots for the control and target devices.

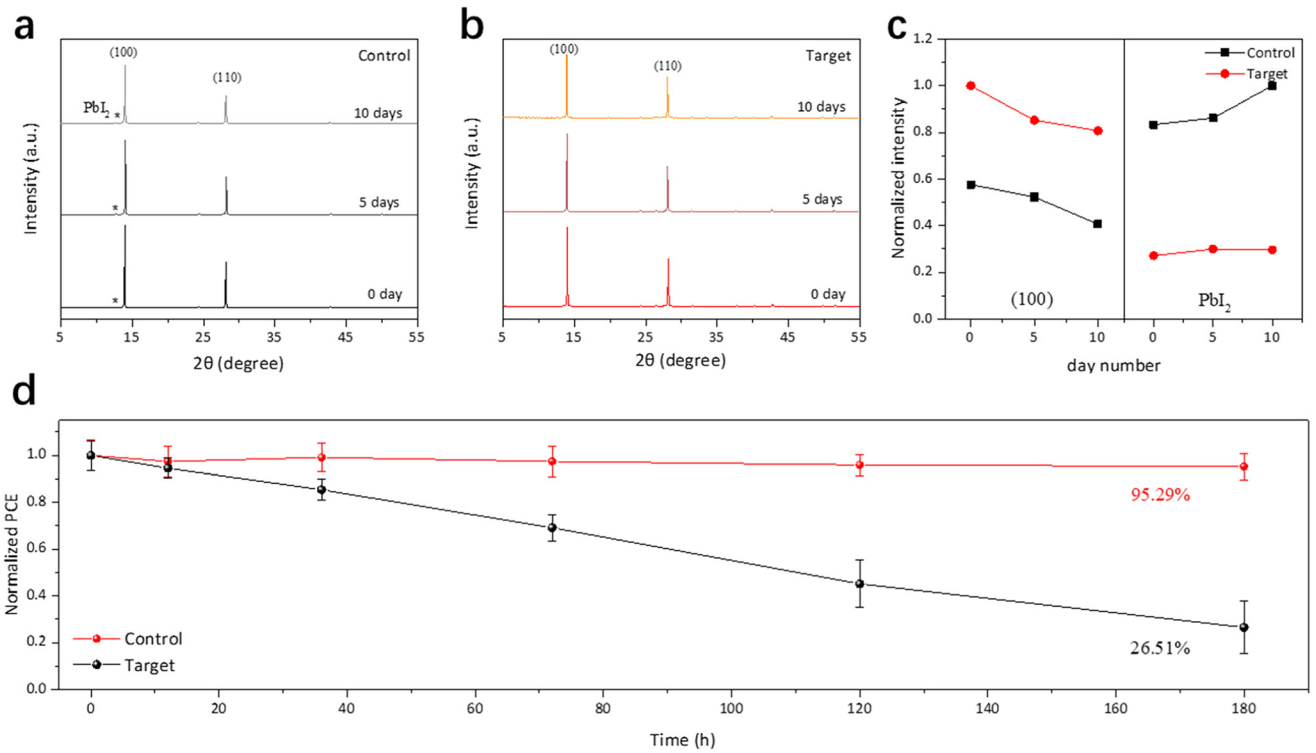

Fig. 7 The XRD of (a) CBD-SnO_2-PVK and (b) CBD-SSO-PVK at 25 °C under air atmosphere (RH = 25–30%). (c) (100) and PbI_2 peak intensity change with aging days. (d) Stability tests of PSCs stored at 20 °C and 25–30% RH for 180 h.

V), indicating a stronger internal driving force for charge carrier separation and transport in the target device. Devices with different perovskite components were also prepared simultaneously with the same device structure. It can be observed from the device performance parameters presented in Fig. S9 of the ESI† that surface reconstruction of CBD-MO_X positively impacts the device efficiency of various perovskite components, primarily attributed to its influence on interface defect state density and charge transfer behavior.

Ultimately, the stability of perovskite films and PSCs was assessed. Fig. 7a and b depict the XRD of perovskite films under an air atmosphere at 25 °C with a relative humidity (RH) of 30–40%. Fig. 7c presents the normalized statistical diagram illustrating the change in the diffraction peak and PbI_2 peak intensity of control and target perovskite films (100) over aging time. After 10 days, there were no significant PbI_2 (12.6°) peaks observed, nor any notable changes in the intensity of the (100) peak in target samples compared to control films. This indicates that the decomposition of the perovskite in contact with the ETL in the target film is effectively inhibited. The performance of an unpackaged device based on the target ETL was evaluated after 1000 hours of exposure to 20–25% RH at 20 °C, and it maintained a PCE retention rate of 95.29% (Fig. 7d), while the control device only retained 26.51% under identical conditions. This remarkable stability of target devices can be attributed to the more compact and smoother ETL/perovskite interface, as well as fewer defect distributions.

3. Conclusion

In summary, we have developed a simple and efficient strategy to rationally reconstruct the surface microstructure of ETLs prepared by the CBD method. This strategy effectively reduces the density of surface oxygen defects in the ETL and regulates the crystallization kinetics of the perovskite without introducing additional cationic impurities. Combining the XPS test and DFT calculation results, we have observed that H_2SO_4 promotes the conversion of Sn-II to Sn-IV and chemisorbed –OH on the surface of SnO_2 to lattice oxygen. Modification with H_2SO_4 achieves better band alignment between the ETL and perovskite layers due to an upward shift in both the conduction band and Fermi level of SnO_2. Consequently, lower energy barriers are achieved at the ETL/perovskite interface, enabling faster electron extraction. In addition, the strong interaction between SO_4^{2-} and PbI_2 alters the crystallization kinetics of the perovskite, leading to the formation of a perovskite with larger grain size and higher uniformity by retarding the rate of crystallization. PSCs based on CBD-SSO achieved a high PCE of 24.29%, with J_{sc}, V_{oc}, and FF values of 24.29 mA cm^{-2}, 1.23 V, and 81.61%, respectively. The initial efficiency of 95.29% is maintained after storage for 1000 hours (20 °C, 20–25% RH) without any encapsulation. These findings indicate that the rational reconstruction of the surface microstructure strategy plays a beneficial role in expanding the commercial application range of MO_x ETLs prepared *via* the CBD method for large-scale PSCs.

Author contributions

Xinxuan Yang: data curation and writing – original draft; Lexin Wang: data curation, formal analysis, and validation; Meihan Liu: data curation and formal analysis; Jiahui Jin: formal analysis; Lili Yang: investigation; Lin Fan: formal analysis and visualization; Maobin Wei: software and resources; Huilian Liu: investigation; Haoran Chen: project administration and resources; Jinghai Yang: software and supervision; Yulei Chang: software and supervision; Fengyou Wang: writing – review & editing, supervision, conceptualization, and investigation.

Data availability

The data supporting this article have been included as part of the ESI.†

The availability data are listed at the end of the file of ESI† Yang *et al.* docx.

Conflicts of interest

There are no conflicts to declare.

Acknowledgements

The authors gratefully acknowledge the support from the National Key Research and Development Program of China (Grant No. 2021YFA0715603), National Natural Science Foundation of China (Grant No. 62275101, 22075101, 62075217, and 62305329), Program for the Development of Science and Technology of Jilin province (Item No. YDZJ202201ZYTS300), Changchun Science and Technology Bureau (Grant No. 23GZZ06) and the China Postdoctoral Science Foundation (Grant No. 2023M733432).

References

1 NREL chart, **https://www.nrel.gov/pv/interactive-cell-efficiency.html**. (accessed: July 2024).
2 S. Huang, P. Li, J. Wang, J. C.-C. Huang, Q. Xue and N. Fu, Modification of SnO_2 Electron Transport Layer: Brilliant Strategies to Make Perovskite Solar Cells Stronger, *Chem. Eng. J.*, 2022, **439**, 135687.
3 L. Lin, T. W. Jones, T. C. Yang, N. W. Duffy, J. Li, L. Zhao, B. Chi, X. Wang and G. J. Wilson, Inorganic Electron Transport Materials in Perovskite Solar Cells, *Adv. Funct. Mater.*, 2021, **31**, 2008300.

4 L. Zang, C. Zhao, X. Hu, J. Tao, S. Chen and J. Chu, Emerging Trends in Electron Transport Layer Development for Stable and Efficient Perovskite Solar Cells, *Small*, 2024, **20**, 2400807.
5 S. S. Shin, S. J. Lee and S. I. Seok, Metal Oxide Charge Transport Layers for Efficient and Stable Perovskite Solar Cells, *Adv. Funct. Mater.*, 2019, **29**, 1900455.
6 J. Gong, Y. Cui, F. Li and M. Liu, Progress in Surface Modification of SnO_2 Electron Transport Layers for Stable Perovskite Solar Cells, *Small Sci.*, 2023, 2200108.
7 J.-P. Correa-Baena, L. Steier, W. Tress, M. Saliba, S. Neutzner, T. Matsui, F. Giordano, T. J. Jacobsson, A. R. S. Kandada, S. M. Zakeeruddin, A. Petrozza, A. Abate, M. K. Nazeeruddin, M. Grätzel and A. Hagfeldt, A. Highly Efficient Planar Perovskite Solar Cells through Band Alignment Engineering, *Energy Environ. Sci.*, 2015, **8**, 2928–2934.
8 E. H. Anaraki, A. Kermanpur, M. T. Mayer, L. Steier, T. Ahmed, S.-H. Turren-Cruz, J. Seo, J. Luo, S. M. Zakeeruddin, W. R. Tress, T. Edvinsson, M. Grätzel, A. Hagfeldt and J.-P. Correa-Baena, Low-Temperature Nb-Doped SnO_2 Electron-Selective Contact Yields over 20% Efficiency in Planar Perovskite Solar Cells, *ACS Energy Lett.*, 2018, **3**, 773–778.
9 Z. Wu, J. Su, N. Chai, S. Cheng, X. Wang, Z. Zhang, X. Liu, H. Zhong, J. Yang, Z. Wang, J. Liu, X. Li and H. Lin, Periodic Acid Modification of Chemical–Bath Deposited SnO_2 Electron Transport Layers for Perovskite Solar Cells and Mini Modules, *Adv. Sci.*, 2023, **10**, 2300010.
10 E. H. Anaraki, A. Kermanpur, L. Steier, K. Domanski, T. Matsui, W. Tress, M. Saliba, A. Abate, M. Grätzel, A. Hagfeldt and J.-P. Correa-Baena, Highly Efficient and Stable Planar Perovskite Solar Cells by Solution-Processed Tin Oxide, *Energy Environ. Sci.*, 2016, **9**, 3128–3134.
11 J. J. Yoo, G. Seo, M. R. Chua, T. G. Park, Y. Lu, F. Rotermund, Y.-K. Kim, C. S. Moon, N. J. Jeon, J.-P. Correa-Baena, V. Bulović, S. S. Shin, M. G. Bawendi and J. Seo, Perovskite Solar Cells via Improved Carrier Management, *Nature*, 2021, **590**, 587–593.
12 G. Tong, L. K. Ono, Y. Liu, H. Zhang, T. Bu and Y. Qi, Up-Scalable Fabrication of SnO_2 with Multifunctional Interface for High Performance Perovskite Solar Modules, *Nano-Micro Lett.*, 2021, **13**, 155.
13 Y.-S. Jeon, D.-H. Kang, J.-H. Kim and N.-G. Park, Stability and Efficiency Improvement of Perovskite Solar Cells by Surface Hydroxyl Defect Passivation of SnO_2 Layer with 4-Fluorothiophenol, *J. Mater. Chem. A*, 2023, **11**, 3673–3681.
14 Z. He, Y. Hu, G. Sun, W. Song, X. Wang, S. Zhang, J. Wang, M. Wang, T. Sun and Y. Tang, Simultaneous Chemical Crosslinking of SnO_2 and Perovskite for High–Performance Planar Perovskite Solar Cells with Minimized Lead Leakage, *Sol. RRL*, 2022, **6**, 2200567.
15 C. Zhang, H. Wang, H. Li, Q. Zhuang, C. Gong, X. Hu, W. Cai, S. Zhao, J. Chen and Z. Zang, Simultaneous Passivation of Bulk and Interface Defects through Synergistic Effect of Anion and Cation toward Efficient and Stable Planar Perovskite Solar Cells, *J. Energy Chem.*, 2021, **63**, 452–460.
16 W. Hou, M. Guo, Y. Chang, S. Zhu, H. Bi, Q. Shen, Y. Xiao and G. Han, In Situ Lead Oxysalt Passivation Layer for Stable and Efficient Perovskite Solar Cells, *Chem. Commun.*, 2022, **10**, 1039.
17 J. Liu, Y. Yin, B. He, P. Wang, M. Wang, X. Cai, Y. Han, Z. Su, J. Gao, R. Cai, S. Jin, X. Gao, J. Bian and Y. Shi, Focusing on the Bottom Contact: Carbon Quantum Dots Embedded SnO_2 Electron Transport Layer for High-Performance and Stable Perovskite Solar Cells, *Mater. Today Phys.*, 2023, **33**, 101041.
18 D. Wang, X. Guo, G. Zhang, Y. Liu, S. Liu, Z. Zhang, Y. Chai, Y. Chen, J. Zhang and B. Sun, SnO_2 Electron Transport Layer Modified by F/N-Doped Graphdiyne and in Situ XRD and in Situ XAFS Exploration on Its Effect on Perovskite Active Layer, *Nano Today*, 2023, **50**, 101852.
19 H. Min, D. Y. Lee, J. Kim, G. Kim, K. S. Lee, J. Kim, M. J. Paik, Y. K. Kim, K. S. Kim, M. G. Kim, T. J. Shin and S. Il Seok, Perovskite Solar Cells with Atomically Coherent Interlayers on SnO_2 Electrodes, *Nature*, 2021, **598**, 444–450.
20 J. Zhang, C. Bai, W. Shen, Q. Zhang, F. Huang, Y.-B. Cheng and J. Zhong, Batch Chemical Bath Deposition of Large-Area SnO_2 Film with Mercaptosuccinic Acid Decoration for Homogenized and Efficient Perovskite Solar Cells, *Chem. Eng. J.*, 2021, **425**, 131444.
21 E. H. Jung, B. Chen, K. Bertens, M. Vafaie, S. Teale, A. Proppe, Y. Hou, T. Zhu, C. Zheng and E. H. Sargent, Bifunctional Surface Engineering on SnO_2 Reduces Energy Loss in Perovskite Solar Cells, *ACS Energy Lett.*, 2020, **5**, 2796–2801.
22 Z. Q. Lin, H. J. Lian, B. Ge, Z. Zhou, H. Yuan, Y. Hou, S. Yang and H. G. Yang, Mediating the Local Oxygen-Bridge Interactions of Oxysalt/Perovskite Interface for Defect Passivation of Perovskite Photovoltaics, *Nano-Micro Lett.*, 2021, **13**, 177.
23 C. Zhan, C. Luo, F. Gao, X. Wang and Q. Zhao, Indium Tin Oxide Induced Internal Positive Feedback and Indium Ion Transport in Perovskite Solar Cells, *Angew. Chem., Int. Ed.*, 2024, **22**, 30.
24 T. Singh, S. Öz, A. Sasinska, R. Frohnhoven, S. Mathur and T. Miyasaka, Sulfate–Assisted Interfacial Engineering for High Yield and Efficiency of Triple Cation Perovskite Solar Cells with Alkali–Doped TiO_2 Electron–Transporting Layers, *Adv. Funct. Mater.*, 2018, **28**, 1706287.
25 L. Yang, J. Feng, Z. Liu, Y. Duan, S. Zhan, S. Yang, K. He, Y. Li, Y. Zhou, N. Yuan and J. Ding, Record–Efficiency Flexible Perovskite Solar Cells Enabled by Multifunctional Organic Ions Interface Passivation, *Adv. Mater.*, 2022, 2201681.
26 Y. Ai, Y. Zhang, J. Song, T. Kong, Y. Li, H. Xie and D. Bi, In Situ Perovskitoid Engineering at SnO_2 Interface toward Highly Efficient and Stable Formamidinium Lead Triiodide Perovskite Solar Cells, *J. Phys. Chem. Lett.*, 2021, **12**, 10567–10573.
27 J. Jia, C. Qian, Y. Dong, Y. F. Li, H. Wang, M. Ghoussoub, K. T. Butler, A. Walsh and G. A. Ozin, Heterogeneous

Catalytic Hydrogenation of CO_2 by Metal Oxides: Defect Engineering – Perfecting Imperfection, *Chem. Soc. Rev.*, 2017, 4631–4644.

28 J. Jia, C. Qian, Y. Dong, Y. F. Li, H. Wang, M. Ghoussoub, K. T. Butler, A. Walsh and G. A. Ozin, Heterogeneous catalytic hydrogenation of CO_2 by metal oxides: defect engineering – perfecting imperfection, *Chem. Soc. Rev.*, 2017, **46**, 4631–4644.

29 C. Qiu, Y. Song, H.-X. Deng and S.-H. Wei, Dual-Level Enhanced Nonradiative Carrier Recombination in Wide-Gap Semiconductors: The Case of Oxygen Vacancy in SiO_2, *J. Am. Chem. Soc.*, 2023, **145**, 24952–24957.

30 K. G. Godinho, A. Walsh and G. W. Watson, Energetic and Electronic Structure Analysis of Intrinsic Defects in SnO_2, *J. Phys. Chem. C*, 2009, **113**, 439–448.

31 Z. Qin, Y. Chen, X. Wang, N. Wei, X. Liu, H. Chen, Y. Miao and Y. Zhao, Zwitterion–Functionalized SnO_2 Substrate Induced Sequential Deposition of Black–Phase $FAPbI_3$ with Rearranged PbI_2 Residue, *Adv. Mater.*, 2022, 2203143.

32 Z. Wu, X. Liu, H. Zhong, Z. Wu, H. Chen, J. Su, Y. Xu, X. Wang, X. Li and H. Lin, Natural Amino Acid Enables Scalable Fabrication of High–Performance Flexible Perovskite Solar Cells and Modules with Areas over 300 Cm^2, *Small Methods*, 2022, 220069.

33 J. Deng, H. Zhang, K. Wei, Y. Xiao, C. Zhang, L. Yang, X. Zhang, D. Wu, Y. Yang and J. Zhang, Molecular Bridge Assisted Bifacial Defect Healing Enables Low Energy Loss for Efficient and Stable Perovskite Solar Cells, *Adv. Funct. Mater.*, 2022, 2209516.

34 Z. Huang, Y. Bai, X. Huang, L. Jiatong, Y. Wu, Y. Chen, K. Li, X. Niu, N. Li, G. Liu, Y. Zhang, H. Zai, Q. Chen, T. Lei, L. Wang and H. Zhou, Anion–π Interactions Suppress Phase Impurities in $FAPbI_3$ Solar Cells, *Nature*, 2023, **623**, 531–537.